



Earth's Future

RESEARCH ARTICLE

10.1029/2022EF003275

Key Points:

- A PV perspective concisely explains how extratropical oceans and the Arctic remotely influence the land temperature
- PV fronts and jet streams jointly constrain the preferred land regions influenced by oceans and the Arctic
- The PV perspective holds for both mean climate change and high-frequency weather variability

Supporting Information:

Supporting Information may be found in the online version of this article.

Correspondence to:

Y. Xie,
xieyk@lzu.edu.cn

Citation:

Xie, Y., Huang, J., Wu, G., & Liu, Y. (2023). Potential vorticity dynamics explain how extratropical oceans and the Arctic modulate wintertime land-temperature variations. *Earth's Future*, 11, e2022EF003275. <https://doi.org/10.1029/2022EF003275>

Received 13 OCT 2022

Accepted 22 JAN 2023

Author Contributions:

Conceptualization: Yongkun Xie
Formal analysis: Yongkun Xie, Jianping Huang, Guoxiong Wu, Yimin Liu
Funding acquisition: Jianping Huang
Investigation: Yongkun Xie, Jianping Huang, Guoxiong Wu, Yimin Liu
Methodology: Yongkun Xie, Jianping Huang
Project Administration: Jianping Huang
Supervision: Jianping Huang, Guoxiong Wu
Validation: Yongkun Xie, Jianping Huang, Yimin Liu
Visualization: Yongkun Xie
Writing – original draft: Yongkun Xie

© 2023 The Authors.

This is an open access article under the terms of the Creative Commons Attribution-NonCommercial License, which permits use, distribution and reproduction in any medium, provided the original work is properly cited and is not used for commercial purposes.

Potential Vorticity Dynamics Explain How Extratropical Oceans and the Arctic Modulate Wintertime Land-Temperature Variations

Yongkun Xie¹ , Jianping Huang¹ , Guoxiong Wu^{2,3} , and Yimin Liu^{2,3} 

¹Collaborative Innovation Center for Western Ecological Safety, Lanzhou University, Lanzhou, China, ²State Key Laboratory of Numerical Modeling for Atmospheric Sciences and Geophysical Fluid Dynamics (LASG), Institute of Atmospheric Physics, Chinese Academy of Sciences, Beijing, China, ³College of Earth and Planetary Sciences, University of Chinese Academy of Sciences, Beijing, China

Abstract Temperature variations across the continental northern hemisphere at the interdecadal scale are thought to be remotely modulated by oceanic internal climate variability and the Arctic. Nevertheless, further elucidating the dynamics is essential for clarifying ongoing debates. We show that potential vorticity (PV) dynamics provide a concise explanation for these teleconnections. Our findings demonstrate that extratropical oceans and the Arctic can remotely modulate the wintertime continental temperature variations by stimulating PV anomalies, which are constrained by climatological PV gradients and jet streams. A causal explanation includes anomalous temperature and precipitation over oceans and the Arctic inducing local PV anomalies via diabatic heating. Subsequently, meridional and downstream advection distributes the anomalous PV to remote land regions where the climatological PV gradients are strong, that is, involving PV fronts, as well as jet streams; therefore, PV fronts and jet streams jointly indicate land regions that are largely and frequently impacted. However, land can also modulate other regions through the same mechanism when variations over land occur in advance. Clear causality depends on which factor is independent, while interactions among those regions may convolute the causality, thereby causing further debates.

Plain Language Summary Studies have indicated the crucial influences of both the oceanic internal climate variability and the Arctic on regional wintertime temperature variations across the continental northern hemisphere at the interdecadal scale. However, a concise explanation of the underlying mechanisms is necessary, especially when causality in the Arctic and mid-latitude connections is under debate. We show that potential vorticity (PV) dynamics can provide a lucid viewpoint. In particular, the findings demonstrate that PV fronts (i.e., regions with strong climatological PV gradients) and jet streams jointly constrain the land regions that are most influenced by oceans and the Arctic. This PV perspective can be applied to general teleconnections over a wide frequency range.

1. Introduction

The Earth's climate is characterized by interdecadal variability (IPCC, 2013), as indicated by interdecadal fluctuations in the global mean temperature under the long-term global warming trend (Trenberth, 2015; Wu et al., 2011). Despite partial contributions from external forcing (Estrada et al., 2013; Solomon et al., 2010), studies have suggested that internal climate variability dominates decadal variability (e.g., Mann et al., 2014; Tung & Zhou, 2013; Wallace et al., 1995; Wyatt et al., 2012; Xie et al., 2017). For the northern hemisphere (NH), two of the most crucial internal climate variability modes are the well-known Atlantic multidecadal oscillation (AMO) and Pacific decadal oscillation (PDO); they can explain most (i.e., 84% or higher) of the interdecadal variability in the NH mean temperature, such as (Huang et al., 2017; Li et al., 2013; Steinman et al., 2015). AMO and PDO must be remotely influencing land temperature; otherwise, they would not be able to explain the majority of NH variability. Atmospheric circulation is crucial for sustaining direct connections between the Atlantic and Pacific Oceans and land (Gastineau & Frankignoul, 2015; Huang et al., 2017; Latif & Barnett, 1994).

Temporal temperature variability exhibits also spatial patterns (Cohen et al., 2012; Huang et al., 2017; Kosaka & Xie, 2013). Down-trending interdecadal variability, such as the warming slowdown from 1998 to 2013, is accompanied by widespread cooling over the Eurasian and North American continents (Huang et al., 2017; Kosaka

Writing – review & editing: Yongkun Xie, Jianping Huang, Guoxiong Wu, Yimin Liu

& Xie, 2013). Interdecadal variability in NH temperature is typically more pronounced in winter than it is in summer (Guan et al., 2015; Kosaka & Xie, 2013); thus, this study focuses on winter.

Amplified Arctic warming has been the most prominent characteristic over the last several decades (IPCC, 2013; Screen & Simmonds, 2010; Stouffer & Manabe, 2017), especially since the 1990s (Xie et al., 2022). Some studies have suggested that the Arctic warming is crucial for the Eurasian cooling (Kretschmer et al., 2016; Mori et al., 2014, 2019; Xie et al., 2020, 2022; Zhang et al., 2018), while some studies have suggested a minimal influence of the Arctic on mid-latitudes (Blackport et al., 2019; Blackport & Screen, 2020; Dai & Song, 2020). Clarifying this debate requires a thorough understanding of how interdecadal internal climate variability and persistent Arctic warming jointly affect the land.

In addition to anthropogenic greenhouse-gas forcing (Dai et al., 2019; Notz & Stroeve, 2016; Stroeve et al., 2007; Xie et al., 2019), internal climate variability has been suggested to substantially (i.e., 40%–50%) affect the observed Arctic sea-ice loss (Ding et al., 2019). The oceanic internal climate variability pertaining to the Atlantic and Pacific Oceans also affects the Arctic climate change through both direct atmospheric heat advection and longwave radiation feedback induced by moisture advection (Luo et al., 2017, 2018; Svendsen et al., 2018). Consequently, the observed Arctic climate change already involves internal climate variability signals; therefore, this study focuses on how the PDO, AMO, and Arctic build their connections with land-temperature variations through atmospheric dynamics, rather than the strict cause-and-effect relationships among the four factors. In particular, this study investigates how the omnipresence of connections among the four factors is established by the intrinsic characteristics of the atmosphere.

Potential vorticity (PV) dynamics were used because PV is fundamental regarding atmospheric circulation, such as PV gradients are fundamental regarding the existence of Rossby waves (Hoskins et al., 1985; Wirth et al., 2018). In particular, PV has shed light on the dynamic connections between the Arctic and mid-latitudes, such as the intervention of Arctic warming on atmospheric blocking through meridional PV gradients (Luo et al., 2018), and mechanisms involving PV generation through Arctic warming and further PV advection to mid-latitudes (Xie et al., 2020). The remainder of this paper is organized as follows. Section 2 introduces the data and methods. The results are presented in Section 3. Section 3.1 addresses the observed characteristics of the decadal climate variability. Section 3.2 elaborates on the direct influence of surface heating on the atmospheric circulation. Section 3.3 further addresses the characteristics of PV advection and its effect on regional climate change. Conclusions and discussion are presented in Section 4.

2. Data and Methods

2.1. Observational and Reanalysis Data

Near-surface air temperature (T2m) was obtained from GISTEMP version 5 surface temperature analysis data provided by the Goddard Institute for Space Studies/National Aeronautics and Space Administration (GISS/NASA) (Hansen et al., 2010). Sea-surface temperature (SST) was obtained from the Met Office Hadley Center sea-ice and sea-surface temperature data (HadISST1) (Rayner et al., 2003). GISTEMP and HadISST1, with resolutions of $2^\circ \times 2^\circ$ and $1^\circ \times 1^\circ$, were available since 1880 and 1870, respectively. Precipitation was obtained from the CPC Merged Analysis of Precipitation (CMAP) (Xie & Arkin, 1997), Global Precipitation Climatology Project (GPCP) version 2.3 (Adler et al., 2003), and NOAA's PRECipitation REConstruction (PREC) version 1.0 (Chen et al., 2002). These three datasets were provided by the NOAA/OAR/ESRL PSL (Boulder, CO, USA) at a resolution of $2.5^\circ \times 2.5^\circ$. CMAP and GPCP were available since 1979, while PREC was available since 1948.

ERA-interim reanalysis (ERA-I) data were provided by the European Center for Medium-Range Weather Forecasts (ECMWF) (Dee et al., 2011). We used both pressure- and single-level surface data in a $1.5^\circ \times 1.5^\circ$ horizontal resolution, with the pressure-level data having 37 vertical levels. ERA-I data were available from 1979 onward. This study mainly examines data from the satellite era (i.e., 1979 onward) because, in this more recent period, both observational and reanalysis data are more reliable. Furthermore, we examined the NCEP-DOE Reanalysis-2 (NCEP-2) monthly diabatic heating of the atmosphere at the sigma level. The NCEP-2 provides six components of diabatic heating, namely due to solar radiation, longwave radiation, large-scale condensation, shallow convection, deep convection, and vertical diffusion (Kanamitsu et al., 2002). NCEP-2 is available in a global T62 Gaussian grid with 28 vertical sigma levels from January 1979 to August 2014. All data are monthly means except for the 6-hourly data involved in the calculations of PV and its advection, owing to their nonlinearity.

2.2. Indices of Oceanic Internal Climate Variability Modes

The AMO and PDO indices were calculated from HadISST1 data using the methods proposed by Trenberth and Shea (2006) and Mantua et al. (1997). Specifically, the AMO was indexed using regional mean SST anomalies averaged over regions within 0°–70°N and 0°–80°W with respect to the global mean SST; the PDO was indexed as the time series of the first empirical orthogonal function (EOF) pattern of monthly SST over the domain defined by 20°–70°N and 110°E–100°W, while also removing the global mean SST series from the grids.

2.3. PV, PV Equation, and PV Advection

In this study, we used quasi-geostrophic PV, hereafter referred to as PV (Charney & Stern, 1962). The PV in isobaric coordinates is

$$q = f + \frac{1}{f_0} \nabla^2 \Phi + \frac{\partial}{\partial p} \left(\frac{f_0}{S} \frac{\partial \Phi}{\partial p} \right), \quad (1)$$

where Φ is the geopotential, f is the Coriolis parameter, f_0 is the value of f at 45° N, ∇^2 is the horizontal Laplacian operator, and S indicates the mean static stability over the regions north of 10°N. The expansion of the static stability term is

$$\frac{\partial}{\partial p} \left(\frac{f_0}{S} \frac{\partial \Phi}{\partial p} \right) = -\alpha \frac{\partial}{\partial p} \left(\frac{f_0}{S} \right) + \frac{f_0}{S} \left(-\frac{\partial \alpha}{\partial p} \right), \quad (2)$$

where α indicates specific volume, while using the hydrostatic relation $\frac{\partial \Phi}{\partial p} = -\alpha$.

The PV Equation, that is, PV budget, is

$$\frac{\partial q}{\partial t} = -\mathbf{V} \cdot \nabla q - f_0 \frac{\partial Q_p}{\partial p} + \mathbf{k} \cdot \nabla \times \mathbf{F}, \quad (3)$$

where \mathbf{V} , \mathbf{k} , and \mathbf{F} indicate the horizontal wind-velocity vector, unit vector for the z -direction, and horizontal frictional force, respectively; Q_p indicates the diabatic heating of the atmosphere formulated as $c_p \rho Q$, where Q indicates the widely used diabatic heating in units of K s⁻¹, c_p indicates the specific heat of dry air at constant pressure, and ρ indicates the density of air. The local PV can only be changed by diabatic heating ($-f_0^{-1} \frac{\partial Q}{\partial p}$) and PV advection ($-\mathbf{V} \cdot \nabla q$) when friction is neglected. The PV equation becomes $\frac{dq}{dt} = \frac{\partial q}{\partial t} + \mathbf{V} \cdot \nabla q = 0$ when both diabatic heating and friction are neglected, thereby representing the Lagrangian PV-conservation situation. Nonetheless, the local PV could change owing to the redistribution through PV advection. This PV-conservation equation in an equilibrium (i.e., $\frac{\partial q}{\partial t} \equiv 0$) state is $\mathbf{V} \cdot \nabla q = 0$ and its classic small-perturbation approximation is

$$-\mathbf{V}' \cdot \nabla \bar{q} - \bar{\mathbf{V}} \cdot \nabla q' - \mathbf{V}' \cdot \nabla q' \approx 0, \quad (4)$$

where high-order covariance terms are neglected. Bar and prime symbols indicate the mean and change (e.g., linear trend) over a period, respectively.

The norm of PV gradient is

$$|\nabla \bar{q}| = \sqrt{\left(\frac{\partial \bar{q}}{\partial x} \right)^2 + \left(\frac{\partial \bar{q}}{\partial y} \right)^2}. \quad (5)$$

In addition, regarding synoptic potential temperature variations generated by horizontal advection (Lutsko et al., 2019; Schneider et al., 2015), synoptic PV variability based on the Taylor expansion is formulated as follows:

$$\overline{q'^2} \approx \overline{\left(\frac{\partial \bar{q}}{\partial x} \right)^2 L_x'^2} + \overline{\left(\frac{\partial \bar{q}}{\partial y} \right)^2 L_y'^2} + 2 \overline{\left(\frac{\partial \bar{q}}{\partial x} \right) L_x' \left(\frac{\partial \bar{q}}{\partial y} \right) L_y'} + \dots \quad (6)$$

Lanczos band-pass filtering (Duchon, 1979) was used to obtain the PV component at frequencies of 3–15 days, representing the synoptic PV variability. The synoptic PV variance ($\overline{q'^2}$) in Equation 6 was subsequently calculated using the PV after band-pass filtering.

2.4. PV Inversion

PV inversion is based on an idea resembling that of the electric field–electric charge relation, in which PV is equivalent to the electric charge and other atmospheric field variables are equivalent to the electric field (Davis & Emanuel, 1991; Hartley et al., 1998; Hoskins et al., 1985; Schneider et al., 2003). A detailed theoretical explanation is that the PV anomaly can be expressed in the form of $q' = L(\Phi')$, where $L = \frac{1}{f_0} \nabla^2 + \frac{\partial}{\partial p} \left(\frac{f_0}{S} \frac{\partial}{\partial p} \right)$; the inversion is then described by $\Phi' = L^{-1}(q')$, while the piecewise inversion, that is, $\Phi'_n = L^{-1}(q'_n)$, is allowed because the superposition principle is guaranteed for the linear operator L . The latter can be solved numerically following Davis and Emanuel (1991) or Xie et al. (2020). Because PV inversion occurs across the entire NH north of 10°N, there is no boundary between the west and east (Hartley et al., 1998). Instead of widely used zero-lateral boundary conditions, geopotential anomalies at the lateral boundaries were set by portioning the observed values to each piece based on the percentages. For the north (south) boundary, the percentage at each piece was calculated as the regional mean geopotential anomaly north of 80°N (10°–20°N) from the inversion with zero-lateral boundary conditions relative to the observed values. Our conclusions are insensitive to the lateral boundary conditions. The vertical levels and horizontal grids for the inversion depend on the dataset used, that is, the same as ERA-I data in this study. For details on the boundary conditions at the top and bottom, we refer to the caption of Figure 3.

2.5. Linear Trends and Adjusted P-Values

Linear trends were calculated through linear regressions based on the least-squares method. The corresponding significances were estimated using two-tailed Student's *t*-test. Since we examined the linear trends spatially, the *P*-values of the significance tests were adjusted based on the false discovery rate (FDR) concept (Benjamini & Hochberg, 1995). FDR-adjusted *P*-values were formulated as follows:

$$P_{adj} = P \times \frac{N}{\text{Rank}(P)}, \quad (7)$$

where *N* indicates the total number of grids on the map, that is, in this study, the number of grids north of 10°N, and Rank(*P*) indicates the rank of *P* starting from 1 when all *P*-values are sorted in ascending order. The statistical significance level in this study was set to 95% (i.e., $P_{adj} < 0.05$).

2.6. Vertical Integral of Diabatic Heating

Column-integrated diabatic heating was calculated using NCEP-2 data. The diabatic heating *Q* from NCEP-2 was weighted by $c_p \rho$, so that the unit of the column-integrated diabatic heating is W m^{-2} . The vertical integral of diabatic heating calculated from the NCEP-2 sigma-level data is formulated as

$$[Q] = \int_0^{\infty} c_p \rho Q dz = - \int_{\sigma_S}^{\sigma_T} \frac{c_p p_s Q}{g} d\sigma, \quad (8)$$

where p_s indicates surface pressure, σ indicates the sigma value of vertical levels of NCEP-2 data, and σ_S and σ_T indicate the sigma values at the surface and top of the atmosphere, respectively.

3. Results

3.1. Observed Characteristics of Decadal Climate Variability

Because reanalysis data were available since 1979, the study period was limited to 1979–2010, wherein 2010 was the turning point of the PDO and AMO phases. During 1979–2010, PDO and AMO were in the down-trending and up-trending phases, respectively (Figures S1a and S1b in Supporting Information S1), thereby causing the linear trends in NH SST to exhibit significant (i.e., $P_{adj} < 0.05$; Section 2.5) patterns of negative PDO and positive AMO phases (Figure 1a and Figure S1c in Supporting Information S1). The near-surface air temperature over the Pacific and Atlantic Oceans (Figure 1b) exhibited patterns similar to those of SST (Figure 1a). Because SST in ice-covered regions was unavailable (Figure 1a), Arctic amplification was the most prominent characteristic of near-surface air temperature trends in the NH (Figure 1b), including the overall Arctic amplification (i.e., amplified warming across the entire Arctic relative to lower latitudes) and regional Arctic amplifications in two regions, namely the north of Barents sea (NBS; from Franz Josef Land westward to Svalbard Archipelago and

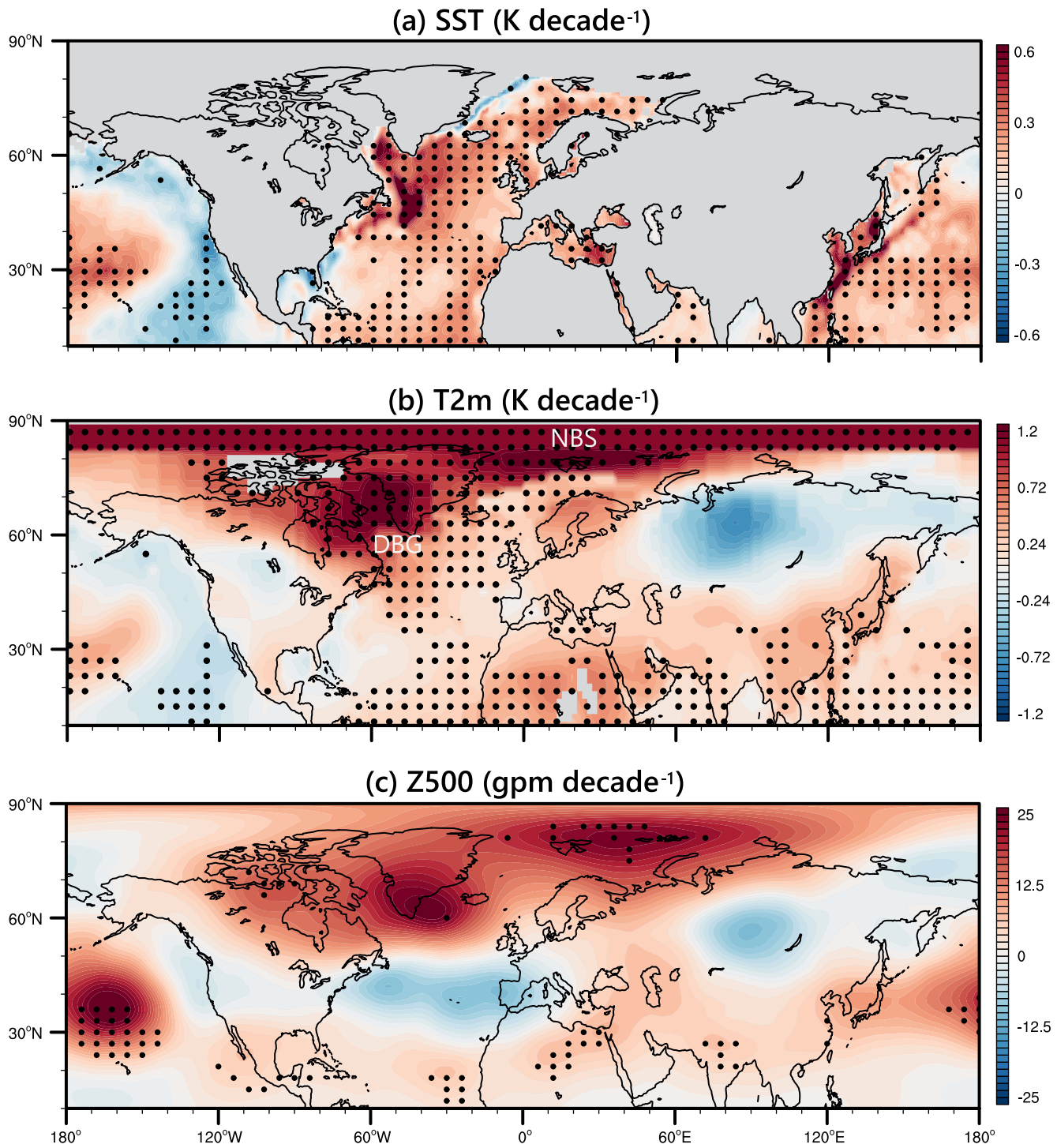


Figure 1. Linear trends in December to February (DJF) mean (a) sea-surface temperature (SST), (b) 2-m near-surface air temperature (T2m), and (c) geopotential height at 500 hPa (i.e., Z500) from 1979 to 2010. Black dots indicate where the linear trends were significant at the 95% significance level (i.e., $P_{adj} < 0.05$; Section 2.5). NBS and DBG in (b) indicate the north of Barents Sea and regions of Davis Strait, Baffin Bay, and southwest of Greenland, respectively. Results pertaining to surface pressure, Z850, and Z300 are shown in Figure S2 in Supporting Information S1.

Greenland Sea), and regions of the Davis Strait, Baffin Bay, and southwest of Greenland (DBG). In addition to the East Pacific Ocean cooling due to the down-trending PDO, cooling was also evident over the two continents, that is, the high latitudes of Eurasia and central North America (Figure 1b). Because the background global warming tends to conceal interdecadal cooling (Huang et al., 2017; Steinman et al., 2015), it is generally harder

for the observed cooling trends to pass the significance test compared to the warming trends; therefore, the interdecadal cooling trends over Eurasia and North America are not statistically significant, although the underlying interdecadal variability of the Earth's climate is robust (Kosaka & Xie, 2013; Trenberth, 2015; Wu et al., 2011).

Overall, the Arctic amplification led to a generally weakened meridional temperature gradient, as well as a pressure gradient (Figures 1b and 1c), between the Arctic and mid-latitudes (Cohen et al., 2020; Francis & Vavrus, 2012). Meanwhile, tropical upper-tropospheric warming amplification caused an enhanced meridional pressure gradient between the tropics and mid-latitudes (Figure S2c in Supporting Information S1; Allen & Sherwood, 2008; Fu et al., 2011; Santer et al., 2005). Therefore, the observed interdecadal trends in geopotential height at 500 hPa (i.e., Z500) exhibited a general positive-negative-positive tripole pattern (Figure 1c), which was also evident in the interannual variability (Liu et al., 2022). Zonal asymmetric anticyclonic/cyclonic circulation centers were also evident, in addition to the general zonal symmetric characteristic (Figure 1c).

Specifically, the down-trending PDO (Figure 1a) induced prominent anticyclonic circulation in the Pacific Ocean (Figure 1c). The anticyclonic circulations in the NBS and DBG (Figure 1c) were associated with regional Arctic amplifications in the two regions (Figure 1b). The cyclonic circulation in the Atlantic Ocean (Figure 1c) was constrained by the up-trending AMO-induced SST, which induced weaker warming in the mid-latitude Atlantic Ocean than on the Arctic and tropical sides (Figure 1a). Meanwhile, cyclonic circulation in Eurasia was associated with Eurasian near-surface cooling (Xie et al., 2020). In addition, the AMO also contributed to the anticyclonic circulation in the DBG because the up-trending AMO-induced high SST in the DBG (Figure 1a) tended to favor Arctic amplification in the DBG (Figure 1b).

Diabatic heating of the atmosphere is the link connecting the oceanic internal climate variability modes and Arctic amplification with the atmospheric circulation (Gill, 1980; Held et al., 2002; Hoskins & Karoly, 1981; Kim et al., 2021). Based on the linear trend in column-integrated diabatic heating (Figure 2a), the PDO, AMO, and regional Arctic amplifications in the NBS and DBG are all associated with anomalous diabatic heating. Overall, the diabatic heating anomalies of the PDO and AMO are dominated by large-scale condensation heating and convective heating (Figure 2b), whereas the diabatic heating anomalies of the two regional Arctic amplifications are dominated by vertical diffusive sensible heating (Figure 2c). Specifically, the down-trending PDO led to a dipole of diabatic heating (Figure 2b) and precipitation (Figure 2d and Figure S3 in Supporting Information S1) in the mid-latitudes, with positive and negative signs in the west and east of the Pacific Ocean, respectively. The up-trending AMO led to significant positive diabatic heating in the mid-latitudes, where insignificant negative trends were evident at the north/south sides (Figure 2b). The positive precipitation anomaly concerning the mid-latitude diabatic heating anomaly was mainly located in the eastern Atlantic Ocean (Figure 2d), whereas a significant negative precipitation anomaly was observed causing a negative diabatic heating anomaly in the north. The two regional Arctic amplifications are tied to dipole diabatic heating induced by vertical diffusion; it is suggested that these dipole patterns are jointly induced by oceanic heating from the Arctic Ocean and two-way interactions between the Arctic and mid-latitudes (Xie et al., 2022). In addition, negative diabatic heating in the DBG is also favored by AMO-induced negative diabatic heating in the north.

3.2. Direct Influence of Surface Heating

Piecewise PV inversion was used to quantify the direct effect of diabatic heating from the Earth's surface. The inversion quantified the geopotential height anomaly induced by an arbitrary piece of anomalous PV (Section 2.4). The surface-PV-anomaly-induced Z500 (Figure 3a) demonstrated the direct effect of surface heating on atmospheric circulation. Specifically, anomalous surface PV induced anticyclonic circulations in the Pacific Ocean, NBS, and DBG, and cyclonic circulation in the mid-latitudes of the Atlantic Ocean (Figure 3a). However, the surface PV anomaly had a minimal contribution to the observed anomalous Z500 over the land regions, except for the eastern Mediterranean (Figure 1c). In contrast, the PV anomaly in the troposphere dominated the anomalous Z500 on land (Figure 3b). Moreover, the tropospheric-PV-anomaly-induced Z500 also substantially contributed to the anomalous Z500 in the two oceans and two regions of Arctic amplification. Therefore, the direct influence of surface PV was generally constrained locally, whereas the tropospheric PV anomaly was directly responsible for the remote influence of oceanic internal climate variability and two regional Arctic amplifications on land.

According to the PV equation (Equation 3), a local PV anomaly can be generated by diabatic heating, friction, and redistribution through PV advection. Furthermore, based on the definition (Equation 1), diabatic heating directly generates PV by changing the static stability, which is dominated by the vertical gradient of the specific

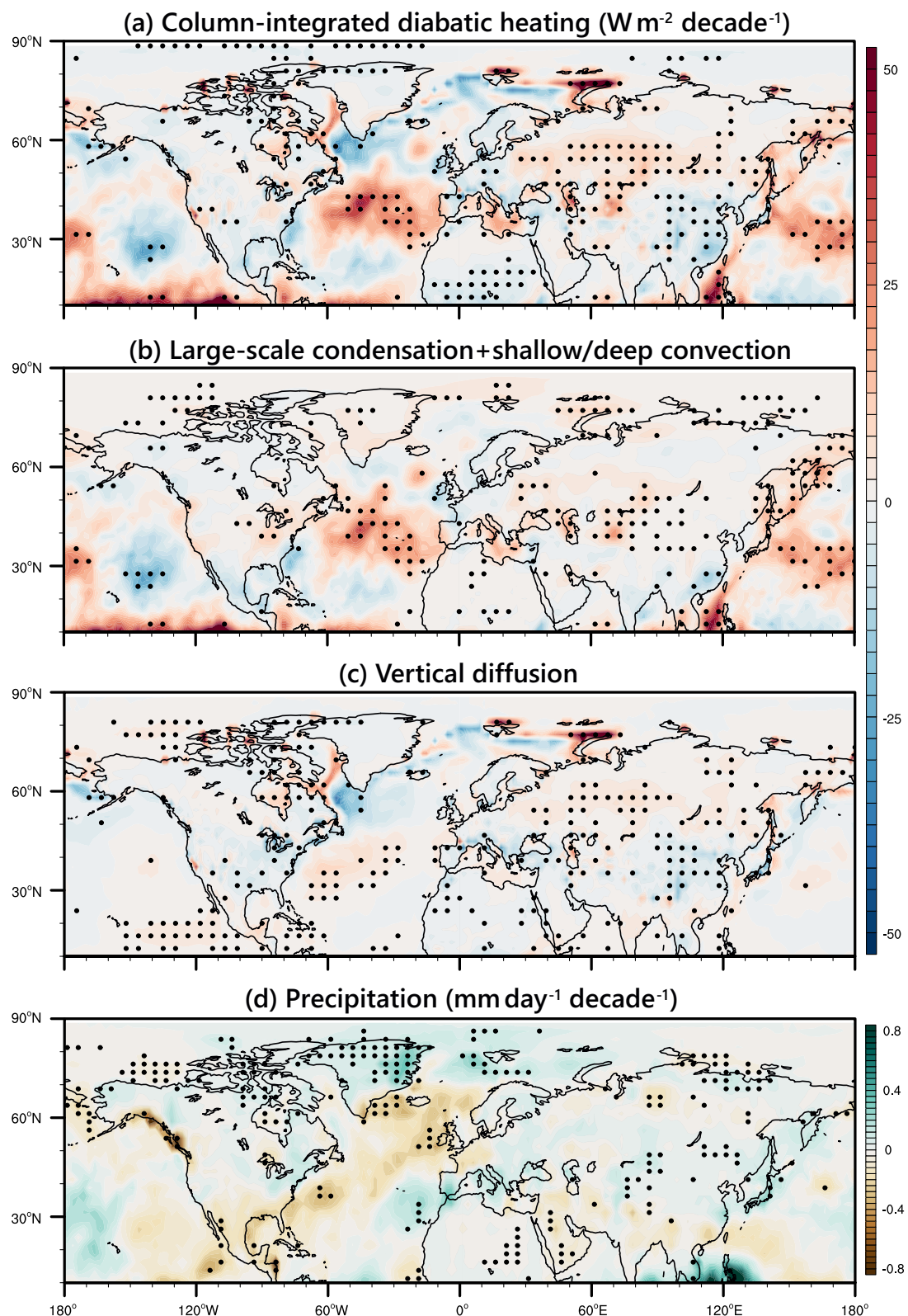


Figure 2. Linear trends in DJF mean (a) column-integrated diabatic heating (Equation (8)) based on NCEP-2 data and its components, (b) the sum of large-scale condensation and shallow/deep convection, (c) vertical diffusion, and (d) precipitation based on the average of CMAP, CPCP, and PREC data from 1979 to 2010. Black dots indicate where the linear trends were significant at the 95% significance level (i.e., $P_{adj} < 0.05$; Section 2.5). Results pertaining to individual CMAP, GPCP, and PREC data are shown in Figure S3 in Supporting Information S1.

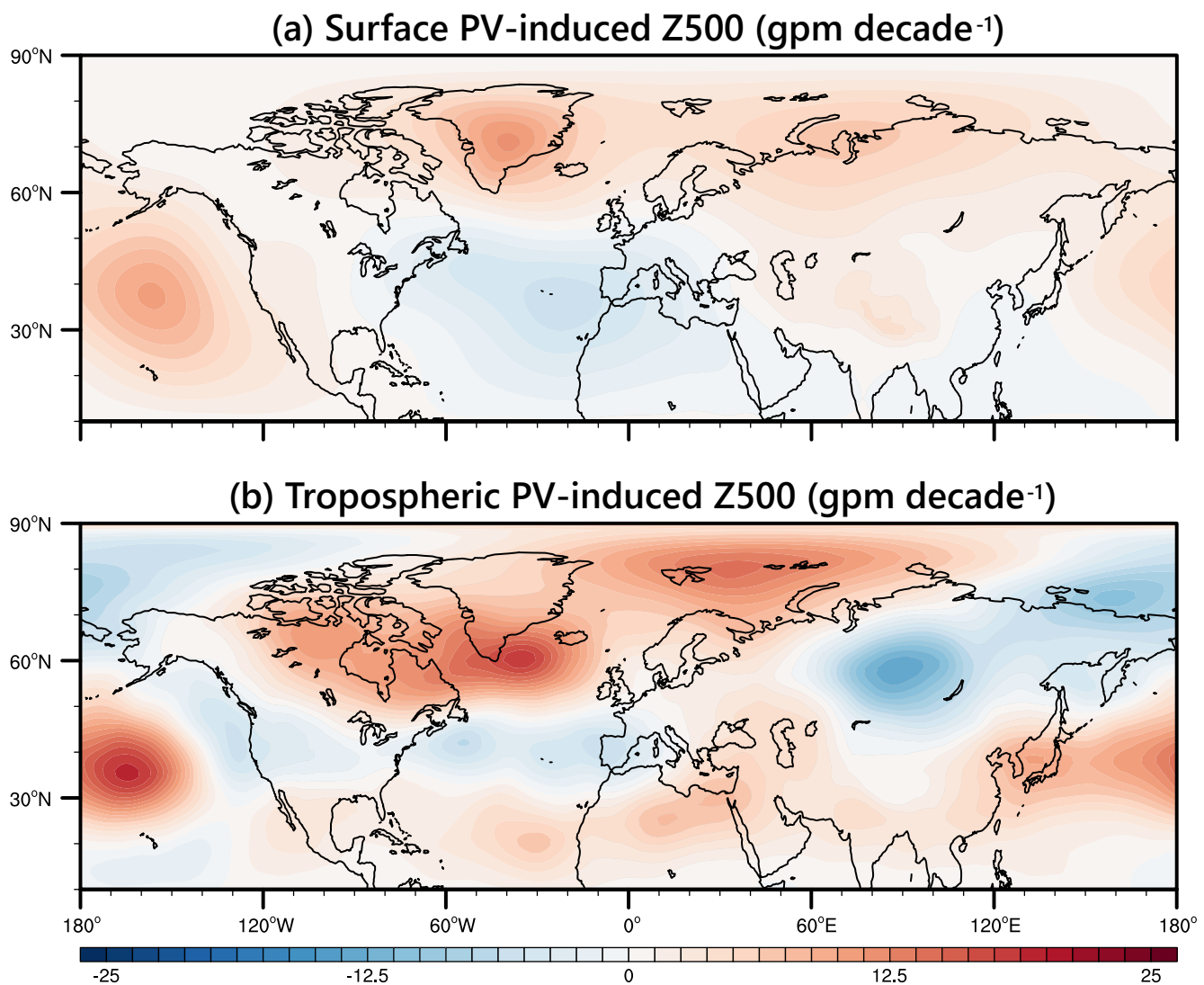


Figure 3. Linear trends in DJF mean Z500 induced by PV anomaly (a) at the surface and (b) in the troposphere, that is, from the surface to 250 hPa, based on a piecewise PV inversion with three pieces. The first piece (a) prescribes observed PV anomaly at the lowest pressure level above the surface, with the bottom and top boundary conditions prescribed as observed and zero geopotential anomalies, respectively; the second piece (b) prescribes observed PV anomaly from the second-lowest pressure level above the surface to 250 hPa, with bottom and top boundary conditions prescribed as zero geopotential anomalies; the third piece (not shown owing to its minimal value) prescribes observed PV anomaly from 225 hPa to the top pressure level, with bottom and top boundary conditions prescribed as zero and observed geopotential anomalies, respectively, while setting zero PV anomalies at other vertical levels except the prescribed levels for each piece.

volume $-\frac{\partial \alpha}{\partial p}$ (Equation 2). The results indicate that anomalous $-\frac{\partial \alpha}{\partial p}$ (Figure 4a) dominated the PV trends at 925 hPa (Figure 4b). Because diffusive heating generally fades with height, positive (negative) diffusive heating generally has a negative (positive) vertical gradient, as well as negative (positive) PV generation. Consequently, the overall Arctic amplification induced negative trends in static stability and PV (Figure 4) owing to a decrease in Arctic warming and diffusive heating with height (Xie et al., 2022). The dipole diffusive diabatic heating in the DBG and NBS (Figure 3c) also induced a dipole pattern, albeit with opposite signs, in the trends of near-surface PV (Figure 4). In addition, positive diffusive heating (Figure 3c) was also responsible for the negative trends in static stability and PV in the mid-latitudes of the Atlantic Ocean (Figure 4). In contrast, increasing diabatic heating due to large-scale condensation and convection with height in the low atmosphere (Figure 3b) induced significant positive PV trends in the mid-latitudes of the Pacific Ocean (Figure 4).

The PV anomalies induced by the vertical gradient of surface heating determined the atmospheric circulation trends near the surface (Figure S2a in Supporting Information S1), which was locally constrained and had

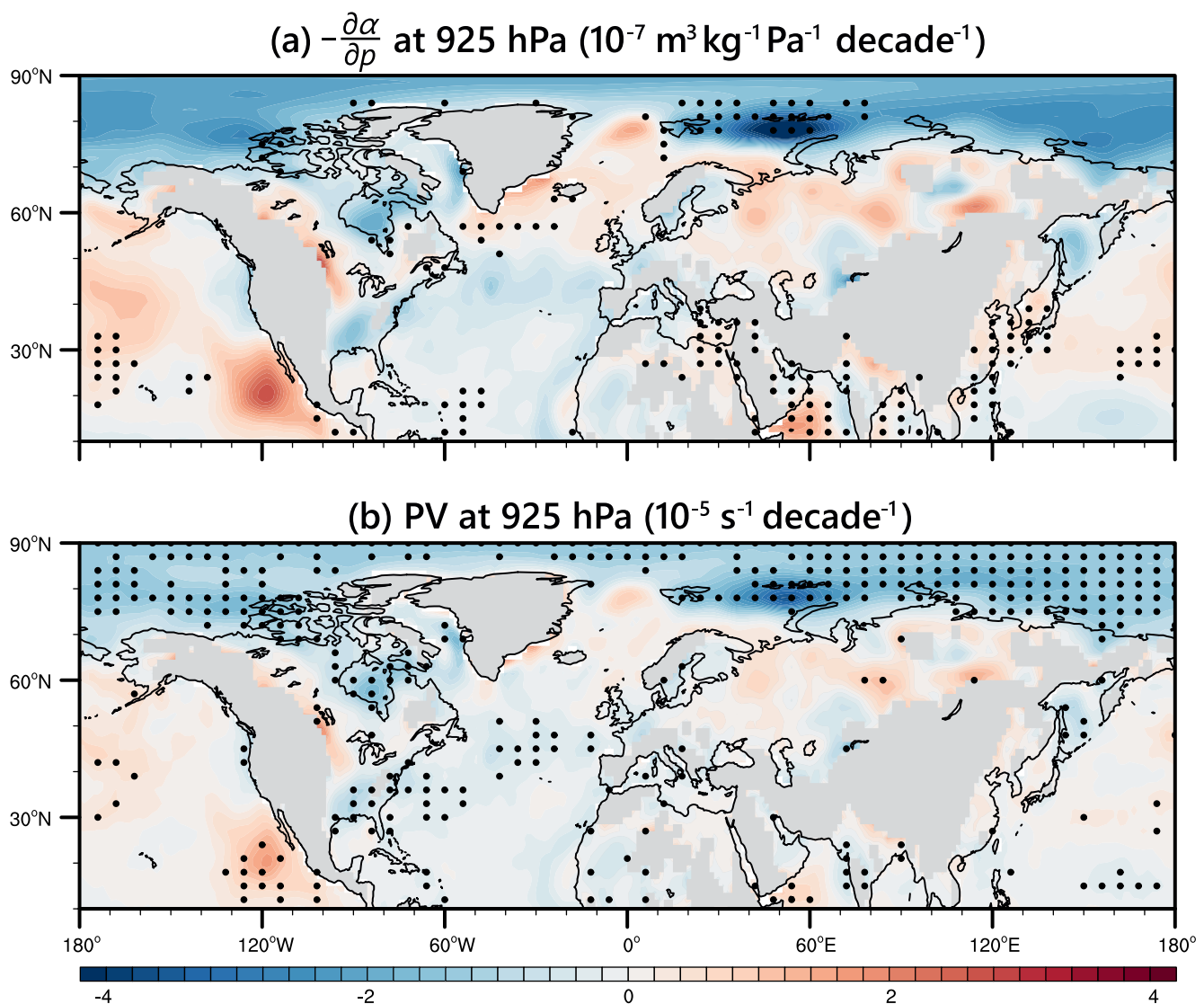


Figure 4. Linear trends in DJF mean (a) vertical gradient of specific volume ($-\frac{\partial \alpha}{\partial p}$; Equation 2) and (b) PV at 925 hPa from 1979 to 2010. Black dots indicate where the linear trends were significant at the 95% significance level (i.e., $P_{adj} < 0.05$; Section 2.5).

little direct contribution to the upper-level atmospheric circulation anomalies pertaining to cooling over land (Figure 3a). In contrast, the redistribution of PV through advection of the interior atmosphere was crucial for the extended influence of the oceans and the Arctic on land, as discussed in the next section.

3.3. Characteristics of PV Advection and Its Effect

PV advection is crucial in the upper troposphere, where diabatic heating and frictional dissipation are weak (Equation (3)). For an equilibrium state close to the Lagrangian PV conservation, the small perturbation-form PV equation can be approximated as Equation (4). Although noise from finite differences exists, the results at 300 hPa indicate that the covariant term is minimal and the balance between the two linear terms $-\nabla' \cdot \nabla \bar{q}$ and $-\bar{V} \cdot \nabla q'$ is prominent (Figure 5). The observed PV trends were determined by the joint effects of the anomalous wind convection of the climatological PV and the climatological wind convection of the anomalous PV. Although Xie et al. (2020) addressed the PV-advection-induced connection between Arctic warming and Eurasian cooling, they did not address the broader connections among oceans, the Arctic, and lands from a PV perspective.

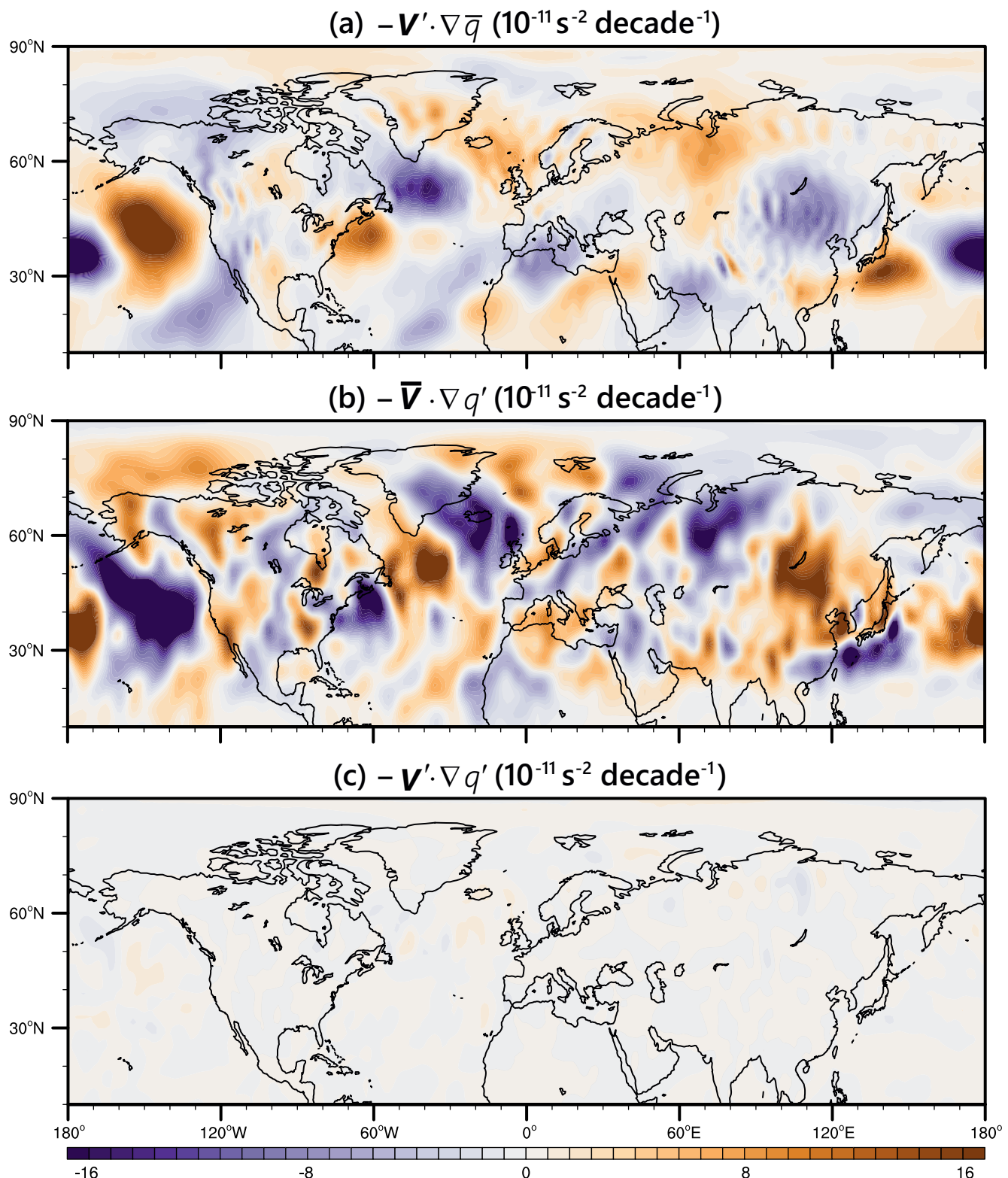


Figure 5. PV advection terms for (a) $-\bar{\mathbf{V}}' \cdot \nabla \bar{q}$, (b) $-\bar{\mathbf{V}} \cdot \nabla q'$, and (c) $-\mathbf{V}' \cdot \nabla q'$ at 300 hPa in Equation (4). The three terms indicate the PV advection contributed by the linear combination of anomalous wind (\mathbf{V}') and climatological PV (\bar{q}), climatological wind ($\bar{\mathbf{V}}$) and anomalous PV (q'), and anomalous wind and PV, respectively (Section 2.3).

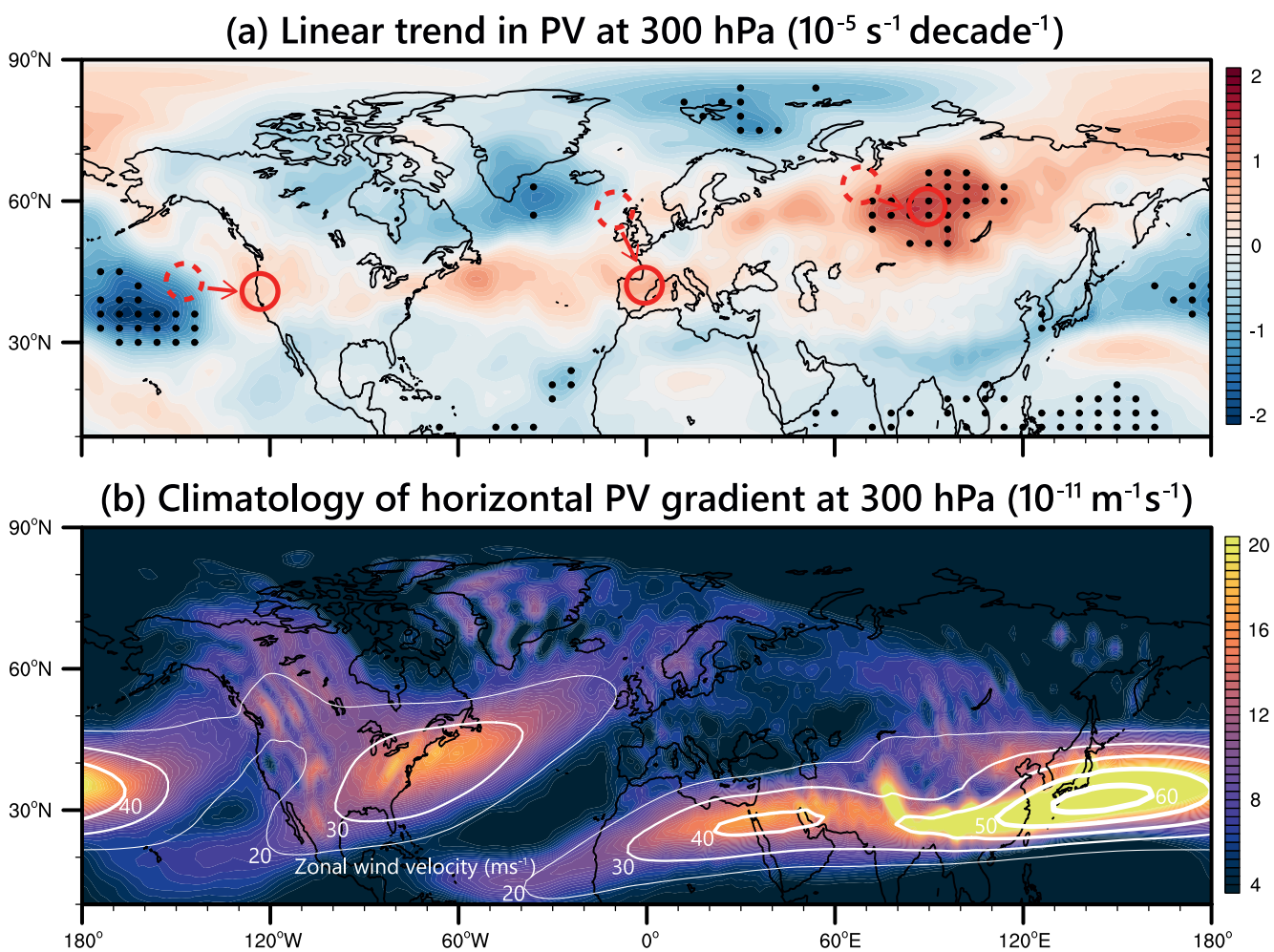


Figure 6. (a) Linear trend in DJF mean PV at 300 hPa from 1979 to 2010. Black dots indicate where the linear trends were significant at the 95% significance level (i.e., $P_{adj} < 0.05$; Section 2.5). Red circles indicate that anomalous wind-adverted positive PV (dashed) was further advected downstream by the climatological wind, thereby causing the observed PV anomaly (solid) over land. (b) Climatology of DJF mean norm of horizontal PV gradient $|\nabla \bar{q}|$ (Equation 5) at 300 hPa for 1979–2010. White contour lines indicate the climatology of the DJF mean zonal wind velocity.

The significant positive PV trends in Siberia (Figure 6a) were jointly induced by the southward positive PV advection due to the anomalous wind and climatological PV (Figure 5a; around the dashed red circle in Figure 6a) and the eastward-positive PV advection due to climatological wind and anomalous PV (Figure 5b) downstream (around the solid circle in Figure 6a). Although statistically insignificant, the positive PV anomalies in North America and Europe (Figure 6a) were also induced by PV advection, similar to that in Siberia. Similarly, PV advection was also crucial for PV trends over the oceans and Arctic. The significant negative PV trends in the mid-latitude Pacific Ocean (Figure 6a) were attributed to negative PV advection due to anomalous wind and climatological PV, and downstream advection of the negative PV due to climatological wind (Figures 5a and 5b). Nonetheless, convective diabatic heating in the Pacific Ocean (Figure 2b) tended to generate negative PV in the upper levels higher than the heating maximum, which also facilitated negative PV in the upper troposphere in the Pacific Ocean (Figure 6a). In addition, the negative PV southeast of Greenland (Figure 6a) was induced by the northeastward advection of the negative anomalous wind-adverted PV (Figure 5a) by the climatological wind (Figure 5b). The significant negative PV trends in the NBS were also favored by the northeastward negative PV advection by the climatological wind (Figure 5b).

Because jet streams are generally collocated with strong PV gradients or PV fronts (Figure 6b), jet streams are widely recognized as Rossby waveguides (Wirth et al., 2018). Nonetheless, PV gradients are more fundamental

to the concept of waveguides (Hoskins et al., 1985; Wirth et al., 2018). Prominent PV trends in the upper troposphere (Figure 6a) are generally present along PV fronts (Figure 6b), as well as jet streams; however, PV fronts are more efficient than jet streams in depicting regions with prominent PV trends, such as those in Siberia (Figure 6). In particular, the climatological PV fronts and jet streams (i.e., $\nabla \bar{q}$ and \bar{V} , respectively, in Equation 4) jointly constrain the preferred regions of PV changes induced by PV advection. In addition to PV advection, the PV trends in the Pacific and Atlantic Oceans and the Arctic are generated by diabatic heating (Figure 4), which is fundamentally related to oceanic internal climate variability and greenhouse forcing. Therefore, the chain reactions from diabatic-heating-initiated PV to the advective redistribution of PV toward a balanced PV budget form a concise PV perspective of the remote connections among the oceans, Arctic, and land.

The PV perspective is crucial for high-frequency weather variability. The variance of PV in the synoptic frequency band (Figure 7a), that is, 3–15 days, indicated that high-frequency PV variability was also increased along the climatological PV fronts (Figure 6b). Furthermore, the climatological PV gradients were dominated by the meridional gradient (Figures 7b and 7c), while a large zonal gradient value was only observed over the topography and coastal regions. This means that meridional displacements were more important in generating local PV anomalies through PV advection than horizontal displacements. Analogous to the mixing-length theory of turbulence, the mixing length of PV in the meridional direction at 300 hPa was inferred from Equation 6. The results indicated that small meridional displacements (i.e., small mixing length in Figure 8a) could induce substantial local PV anomalies along the PV fronts (Figures 6a and 7c), whereas only large meridional displacements in the low PV gradient regions could induce local PV anomalies. Moreover, the PV variance in a wide frequency band, that is, from daily to seasonal (Figure 8b), agreed well with the synoptic variability. Therefore, the PV perspective is essential for low-frequency mean climate change and high-frequency weather variability.

4. Discussion and Conclusions

This study investigated the dynamics underlying teleconnections from the extratropical oceans and the Arctic to land, pertaining to the interdecadal variability of temperature in winter (Guan et al., 2015; Kosaka & Xie, 2013; Trenberth, 2015), which boiled down to a concise PV perspective. The PV-centered viewpoint is summarized as follows: Surface temperature anomalies of oceanic internal climate variability, that is, the AMO and PDO, and the Arctic generated anomalous PV near the surface due to vertically non-uniform diabatic heating, such as diffusive heating. Anomalous condensation heating of precipitation related to oceanic internal climate variability also generated anomalous PV in the troposphere. These diabatic heating-generated PV anomalies initiated anomalous circulation, which further stimulated chain reactions of PV advection and the developed downstream PV anomalies, as well as temperature and circulation anomalies over land. In particular, PV fronts and jet streams in the upper troposphere jointly indicated the preferred regions that are remotely influenced by extratropical oceans and the Arctic. The concept of PV fronts accompanied by jet streams is more appropriate than the widely recognized jet-streams-only concept (Coumou et al., 2018; Wirth et al., 2018). In addition to the interdecadal variability, this PV perspective is crucial for high-frequency weather variability.

Although oceans and the Arctic are recognized as drivers of interdecadal variability of the land (Li et al., 2013; Steinman et al., 2015; Wyatt et al., 2012), land can be a driver as well, once prior anomalies occur over land. For example, snow-cover anomalies over the Eurasian continent in autumn can drive anomalous SST in the Pacific Ocean in winter (Li et al., 2016; Ruggieri et al., 2022). Therefore, the fundamental cause-and-effect relationships among the oceans, Arctic, and land depend on the anomalies from which the regions are independent. The combination of additional numerical simulations with the PV perspective in this study would further elucidate the causality among these factors.

In addition to extratropical oceans, tropical influences are also crucial for land-temperature variations, such as the influence of the El Niño–Southern Oscillation (ENSO) in North America and Greenland (Ding et al., 2014). The effect of the PDO is also related to tropical influences (Huang et al., 2017; Kosaka & Xie, 2013). From a PV perspective, tropical influences can also trigger circulation perturbations and stimulate chain reactions of

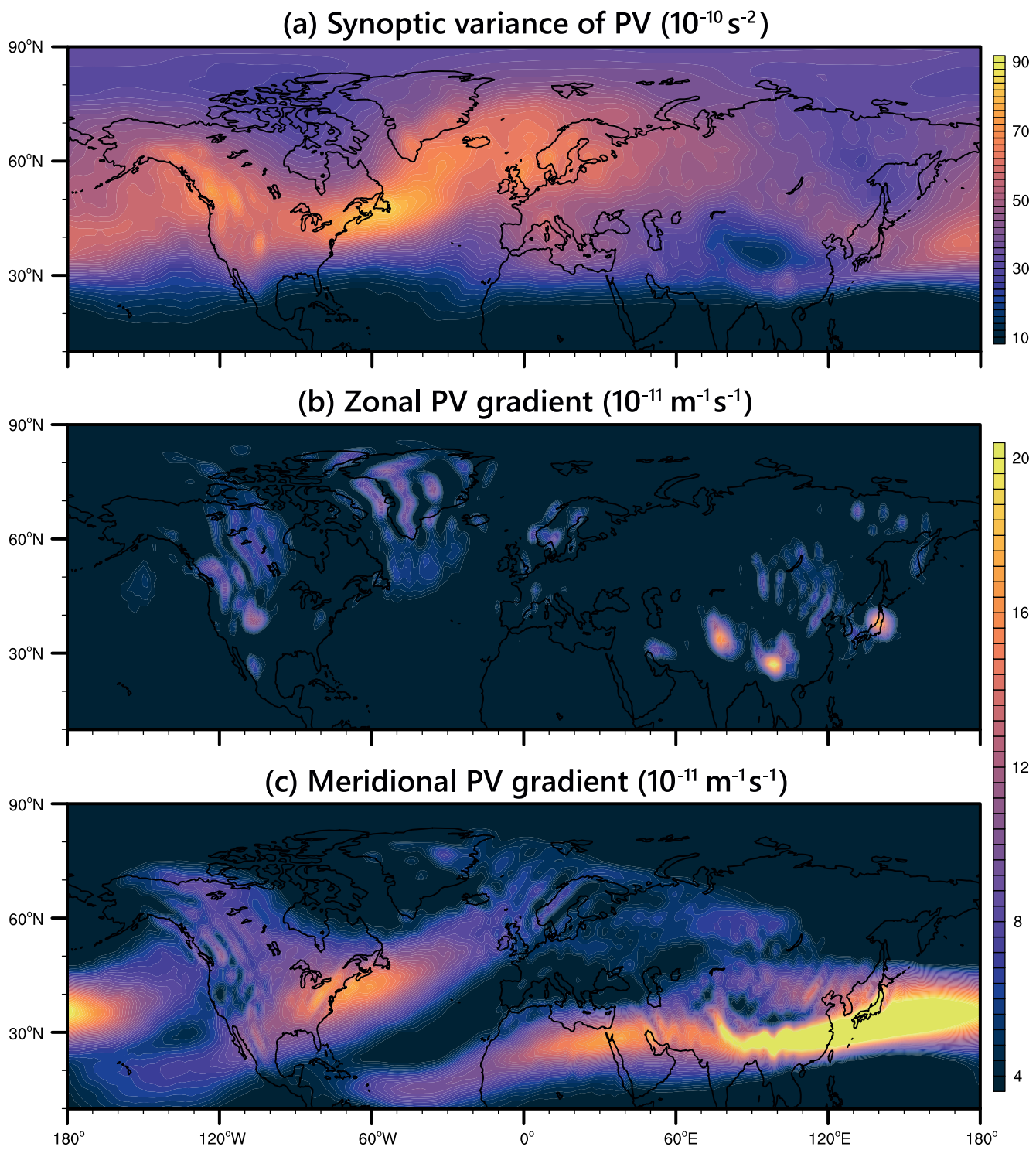


Figure 7. (a) Climatology of PV variance ($\overline{q^2}$; Equation 6) at 300 hPa for the frequency band of synoptic variability (3–15 days; Section 2.3) for 1979–2010. Climatology of the absolute value of the horizontal PV gradient in (b) zonal ($\frac{\partial \overline{q}}{\partial x}$) and (c) meridional ($\frac{\partial \overline{q}}{\partial y}$) direction for 1979–2010.

PV advection that spread over land. Moreover, the dependence on the climatology suggests emergent constraints in climate simulations, which are paramount for performing analyses and projections using models (Eyring et al., 2019; Hill et al., 2017). In practice, climate simulations should also evaluate PV in addition to the widely focused routine variables.

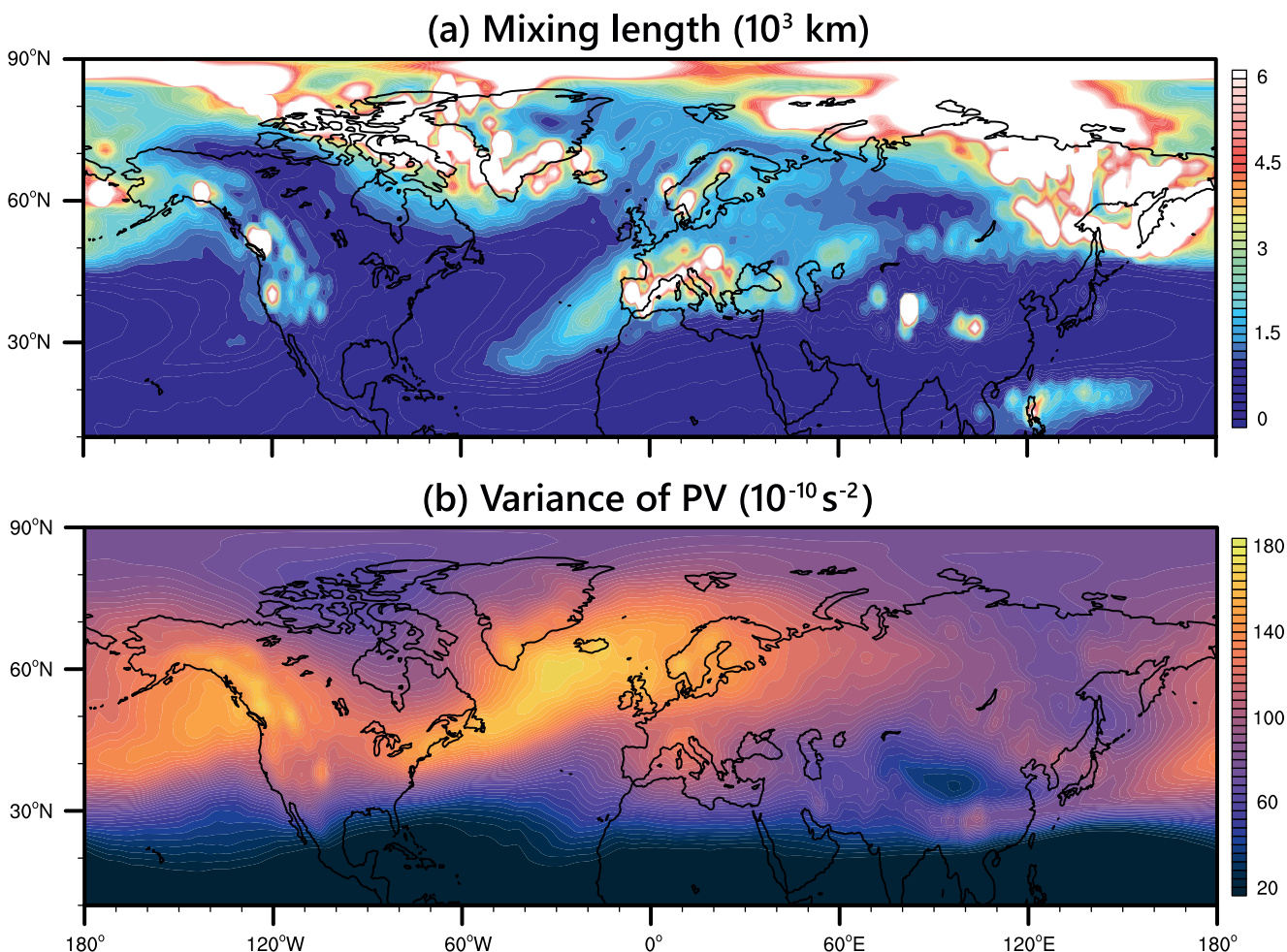


Figure 8. (a) Mixing length of PV in the meridional direction for synoptic variability at 300 hPa, inferred from the formula $\sqrt{L_y'^2} \approx \sqrt{\bar{q}^2 / \left(\frac{\partial \bar{q}}{\partial y} \right)^2}$, which neglects the high-order terms and terms with L_x' in Equation 6, provided that $\frac{\partial \bar{q}}{\partial x} \ll \frac{\partial \bar{q}}{\partial y}$. (b) Climatology of variance of PV (\bar{q}^2) at 300 hPa for frequencies from daily to seasonal for 1979–2010, calculated as the variance of daily PV in DJF after removing the climatological daily mean.

Data Availability Statement

All data examined in this study are publicly available through official websites. GISTEMP data can be accessed at <https://data.giss.nasa.gov/gistemp/>. HadISST1 data are available at <https://www.metoffice.gov.uk/hadobs/hadisst/>. The CMAP, GPCP, and PREC datasets can be accessed at <https://psl.noaa.gov/data/gridded/data.cmap.html>, <https://psl.noaa.gov/data/gridded/data.gpcp.html>, and <https://psl.noaa.gov/data/gridded/data.prec.html>, respectively. The ERA-I data can be accessed at <https://apps.ecmwf.int/datasets/>. The NCEP-2 data are available at <http://iridl.ldeo.columbia.edu/SOURCES/.NOAA/.NCEP-DOE/.Reanalysis-2/.Monthly/.dg3/.dg3/>.

Code Availability Statement: Codes are available from https://github.com/yongkunxie/PVD_OA_L.git.

Acknowledgments

We thank the anonymous reviewers for their constructive comments. We thank GISS/NASA, the Met Office Hadley Centre, NOAA/OAR/ESRL PSL, ECMWF, and NCEP-DOE for making their data available. This work was supported by the National Natural Science Foundation of China (91937302, 42030602) and Gansu Provincial Special Fund Project for Guiding Scientific and Technological Innovation and Development (2019ZX-06).

References

- Adler, R. F., Huffman, G. J., Chang, A. T., Ferraro, R. R., Xie, P., Janowiak, J. E., et al. (2003). The version 2 global precipitation climatology Project (GPCP) monthly precipitation analysis (1979–present). *Journal of Hydrometeorology*, 4(6), 1147–1167. [https://doi.org/10.1175/1525-7541\(2003\)004<1147:tvgpcp>2.0.co;2](https://doi.org/10.1175/1525-7541(2003)004<1147:tvgpcp>2.0.co;2)
- Allen, R. J., & Sherwood, S. C. (2008). Warming maximum in the tropical upper troposphere deduced from thermal winds. *Nature Geoscience*, 1(6), 399–403. <https://doi.org/10.1038/ngeo208>
- Benjamini, Y., & Hochberg, Y. (1995). Controlling the false discovery rate: A practical and powerful approach to multiple testing. *Journal of the Royal Statistical Society: Series B*, 57(1), 289–300. <https://doi.org/10.1111/j.2517-6161.1995.tb02031.x>
- Blackport, R., & Screen, J. A. (2020). Insignificant effect of Arctic amplification on the amplitude of midlatitude atmospheric waves. *Science Advances*, 6(8), eaay2880. <https://doi.org/10.1126/sciadv.aay2880>

- Blackport, R., Screen, J. A., Van der Wiel, K., & Bintanja, R. (2019). Minimal influence of reduced Arctic sea ice on coincident cold winters in mid-latitudes. *Nature Climate Change*, 9, 697–704. <https://doi.org/10.1038/s41558-019-0551-4>
- Charney, J. G., & Stern, M. (1962). On the stability of internal baroclinic jets in a rotating atmosphere. *Journal of the Atmospheric Sciences*, 19(2), 159–172. [https://doi.org/10.1175/1520-0469\(1962\)019<0159:otsoib>2.0.co;2](https://doi.org/10.1175/1520-0469(1962)019<0159:otsoib>2.0.co;2)
- Chen, M., Xie, P., Janowiak, J. E., & Arkin, P. A. (2002). Global land precipitation: A 50-yr monthly analysis based on Gauge observations. *Journal of Hydrometeorology*, 3, 249–266. [https://doi.org/10.1175/1525-7541\(2002\)003<0249:gplaym>2.0.co;2](https://doi.org/10.1175/1525-7541(2002)003<0249:gplaym>2.0.co;2)
- Cohen, J., Zhang, X., Francis, J. A., Jung, T., Kwok, R., Overland, J. E., et al. (2020). Divergent consensuses on Arctic amplification influence on midlatitude severe winter weather. *Nature Climate Change*, 10(1), 20–29. <https://doi.org/10.1038/s41558-019-0662-y>
- Cohen, J. L., Furtado, J. C., Barlow, M., Alexeev, V. A., & Cherry, J. E. (2012). Asymmetric seasonal temperature trends. *Geophysical Research Letters*, 39(4), L04705. <https://doi.org/10.1029/2011gl050582>
- Coumou, D., Di Capua, G., Vavrus, S. J., Wang, L., & Wang, S. (2018). The influence of Arctic amplification on mid-latitude summer circulation. *Nature Communications*, 9(1), 2959. <https://doi.org/10.1038/s41467-018-05256-8>
- Dai, A., Luo, D., Song, M., & Liu, J. (2019). Arctic amplification is caused by sea-ice loss under increasing CO₂. *Nature Communications*, 10(1), 121. <https://doi.org/10.1038/s41467-018-07954-9>
- Dai, A., & Song, M. (2020). Little influence of Arctic amplification on mid-latitude climate. *Nature Climate Change*, 10(3), 231–237. <https://doi.org/10.1038/s41558-020-0694-3>
- Davis, C. A., & Emanuel, K. A. (1991). Potential vorticity diagnostics of cyclogenesis. *Monthly Weather Review*, 119(8), 1929–1953. [https://doi.org/10.1175/1520-0493\(1991\)119<1929:pvdoc>2.0.co;2](https://doi.org/10.1175/1520-0493(1991)119<1929:pvdoc>2.0.co;2)
- Dee, D., Uppala, S. M., Simmons, A., Berrisford, P., Poli, P., Kobayashi, S., et al. (2011). The ERA-interim reanalysis: Configuration and performance of the data assimilation system. *Quarterly Journal of the Royal Meteorological Society*, 137(656), 553–597. <https://doi.org/10.1002/qj.828>
- Ding, Q., Schweiger, A., L'Heureux, M., Steig, E. J., Battisti, D. S., Johnson, N. C., et al. (2019). Fingerprints of internal drivers of Arctic sea ice loss in observations and model simulations. *Nature Geoscience*, 12(1), 28–33. <https://doi.org/10.1038/s41561-018-0256-8>
- Ding, Q., Wallace, J. M., Battisti, D. S., Steig, E. J., Gallant, A. J., Kim, H., & Geng, L. (2014). Tropical forcing of the recent rapid Arctic warming in northeastern Canada and Greenland. *Nature*, 509(7499), 209–212. <https://doi.org/10.1038/nature13260>
- Duchon, C. E. (1979). Lanczos filtering in one and two dimensions. *Journal of Applied Meteorology and Climatology*, 18(8), 1016–1022. [https://doi.org/10.1175/1520-0450\(1979\)018<1016:lfioat>2.0.co;2](https://doi.org/10.1175/1520-0450(1979)018<1016:lfioat>2.0.co;2)
- Estrada, F., Estrada, F., Perron, P., & Martínez-López, B. (2013). Statistically derived contributions of diverse human influences to twentieth-century temperature changes. *Nature Geoscience*, 6(12), 1050–1055. <https://doi.org/10.1038/geo1999>
- Eyring, V., Cox, P. M., Flato, G., Gleckler, P. J., Abramowitz, G., Caldwell, P. M., et al. (2019). Taking climate model evaluation to the next level. *Nature Climate Change*, 9(2), 102–110. <https://doi.org/10.1038/s41558-018-0355-y>
- Francis, J. A., & Vavrus, S. J. (2012). Evidence linking Arctic amplification to extreme weather in mid-latitudes. *Geophysical Research Letters*, 39(6), L06801. <https://doi.org/10.1029/2012gl051000>
- Fu, Q., Manabe, S., & Johanson, C. M. (2011). On the warming in the tropical upper troposphere: Models versus observations. *Geophysical Research Letters*, 38(15), L15704. <https://doi.org/10.1029/2011gl048101>
- Gastineau, G., & Frankignoul, C. J. (2015). Influence of the north Atlantic SST variability on the atmospheric circulation during the twentieth century. *Journal of Climate*, 28(4), 1396–1416. <https://doi.org/10.1175/jcli-d-14-00424.1>
- Gill, A. E. (1980). Some simple solutions for heat-induced tropical circulation. *Quarterly Journal of the Royal Meteorological Society*, 106(449), 447–462. <https://doi.org/10.1002/qj.49710644905>
- Guan, X., Huang, J., Guo, R., & Lin, P. (2015). The role of dynamically induced variability in the recent warming trend slowdown over the northern hemisphere. *Scientific Reports*, 5(1), 12669. <https://doi.org/10.1038/srep12669>
- Hansen, J. E., Ruedy, R., Sato, M., & Lo, K. K. (2010). Global surface temperature change. *Reviews of Geophysics*, 48(4), RG4004. <https://doi.org/10.1029/2010rg000345>
- Hartley, D. E., Villarin, J. T., Black, R. X., & Davis, C. A. (1998). A new perspective on the dynamical link between the stratosphere and troposphere. *Nature*, 391(6666), 471–474. <https://doi.org/10.1038/35112>
- Held, I. M., Ting, M., & Wang, H. (2002). Northern winter stationary waves: Theory and modeling. *Journal of Climate*, 15(16), 2125–2144. [https://doi.org/10.1175/1520-0442\(2002\)015<2125:nwswta>2.0.co;2](https://doi.org/10.1175/1520-0442(2002)015<2125:nwswta>2.0.co;2)
- Hill, S. A., Ming, Y., Held, I. M., & Zhao, M. (2017). A moist static Energy budget-based analysis of the Sahel Rainfall Response to uniform oceanic warming. *Journal of Climate*, 30(15), 5637–5660. <https://doi.org/10.1175/jcli-d-16-0785.1>
- Hoskins, B. J., & Karoly, D. J. (1981). The steady linear response of a spherical atmosphere to thermal and orographic forcing. *Journal of the Atmospheric Sciences*, 38(6), 1179–1196. [https://doi.org/10.1175/1520-0469\(1981\)038<1179:tslroa>2.0.co;2](https://doi.org/10.1175/1520-0469(1981)038<1179:tslroa>2.0.co;2)
- Hoskins, B. J., McIntyre, M., & Robertson, A. W. (1985). On the use and significance of isentropic potential vorticity maps. *Quarterly Journal of the Royal Meteorological Society*, 111(470), 877–946. <https://doi.org/10.1002/qj.49711147002>
- Huang, J., Xie, Y., Guan, X., Li, D., & Ji, F. (2017). The dynamics of the warming hiatus over the northern hemisphere. *Climate Dynamics*, 48(1–2), 429–446. <https://doi.org/10.1007/s00382-016-3085-8>
- IPCC. (2013). *Climate change 2013: The physical science basis. Contribution of working group I to the fifth assessment report of the intergovernmental panel on climate change*. Cambridge University Press.
- Kanamitsu, M., Ebisuzaki, W., Woollen, J. S., Yang, S., Hnilo, J. J., Fiorino, M., & Potter, G. (2002). NCEP–DOE AMIP-II reanalysis (R-2). *Bulletin of the American Meteorological Society*, 83(11), 1631–1643. [https://doi.org/10.1175/bams-83-11-1631\(2002\)083<1631:nar>2.3.co;2](https://doi.org/10.1175/bams-83-11-1631(2002)083<1631:nar>2.3.co;2)
- Kim, D., Kang, S. M., Merlis, T. M., & Shin, Y. (2021). Atmospheric circulation sensitivity to changes in the vertical structure of polar warming. *Geophysical Research Letters*, 48(19), e2021GL094726. <https://doi.org/10.1029/2021gl094726>
- Kosaka, Y., & Xie, S. (2013). Recent global-warming hiatus tied to equatorial Pacific surface cooling. *Nature*, 501(7467), 403–407. <https://doi.org/10.1038/nature12534>
- Kretschmer, M., Coumou, D., Donges, J. F., & Runge, J. (2016). Using causal effect networks to analyze different Arctic drivers of midlatitude winter circulation. *Journal of Climate*, 29(11), 4069–4081. <https://doi.org/10.1175/jcli-d-15-0654.1>
- Latif, M., & Barnett, T. P. (1994). Causes of decadal climate variability over the north Pacific and North America. *Science*, 266(5185), 634–637. <https://doi.org/10.1126/science.266.5185.634>
- Li, H., Wang, H., & Jiang, D. (2016). Influence of October Eurasian snow on winter temperature over Northeast China. *Advances in Atmospheric Sciences*, 34(1), 116–126. <https://doi.org/10.1007/s00376-016-5274-0>
- Li, J., Sun, C., & Jin, F. (2013). NAO implicated as a predictor of northern hemisphere mean temperature multidecadal variability. *Geophysical Research Letters*, 40(20), 5497–5502. <https://doi.org/10.1002/2013gl057877>

- Liu, X., Lu, J., Liu, Y., & Wu, G. (2022). Meridional tripole mode of winter precipitation over the Arctic and continental north Africa–Eurasia. *Journal of Climate*, 34(24), 9665–9678.
- Luo, B., Wu, L., Luo, D., Dai, A., & Simmonds, I. (2018). The winter midlatitude–Arctic interaction: Effects of north Atlantic SST and high-latitude blocking on Arctic sea ice and Eurasian cooling. *Climate Dynamics*, 52(5–6), 2981–3004. <https://doi.org/10.1007/s00382-018-4301-5>
- Luo, D., Chen, Y., Dai, A., Mu, M., Zhang, R., & Ian, S. (2017). Winter Eurasian cooling linked with the Atlantic multidecadal oscillation. *Environmental Research Letters*, 12, 125002. <https://doi.org/10.1088/1748-9326/aa8de8>
- Lutsko, N. J., Baldwin, J. W., & Cronin, T. W. (2019). The impact of large-scale orography on northern hemisphere winter synoptic temperature variability. *Journal of Climate*, 32(18), 5799–5814. <https://doi.org/10.1175/jcli-d-19-0129.1>
- Mann, M. E., Steinman, B. A., & Miller, S. K. (2014). On forced temperature changes, internal variability, and the AMO. *Geophysical Research Letters*, 41(9), 3211–3219. <https://doi.org/10.1002/2014gl059233>
- Mantua, N. J., Hare, S. R., Zhang, Y., Wallace, J. M., & Francis, R. (1997). A Pacific interdecadal climate oscillation with impacts on salmon production. *Bulletin of the American Meteorological Society*, 78(6), 1069–1079. [https://doi.org/10.1175/1520-0477\(1997\)078<1069:apicow>2.0.co;2](https://doi.org/10.1175/1520-0477(1997)078<1069:apicow>2.0.co;2)
- Mori, M., Kosaka, Y., Watanabe, M., Nakamura, H., & Kimoto, M. (2019). A reconciled estimate of the influence of Arctic sea-ice loss on recent Eurasian cooling. *Nature Climate Change*, 9(2), 123–129. <https://doi.org/10.1038/s41558-018-0379-3>
- Mori, M., Watanabe, M., Shiogama, H., Inoue, J., & Kimoto, M. (2014). Robust Arctic sea-ice influence on the frequent Eurasian cold winters in past decades. *Nature Geoscience*, 7(12), 869–873. <https://doi.org/10.1038/ngeo2277>
- Notz, D., & Stroeve, J. C. (2016). Observed Arctic sea-ice loss directly follows anthropogenic CO₂ emission. *Science*, 354(6313), 747–750. <https://doi.org/10.1126/science.aag2345>
- Rayner, N. A., Parker, D. E., Horton, E. B., Folland, C. K., Alexander, L. V., Rowell, D. P., et al. (2003). Global analyses of sea surface temperature, sea ice, and night marine air temperature since the late nineteenth century. *Journal of Geophysical Research*, 108(D14), 4407. <https://doi.org/10.1029/2002jd002670>
- Ruggieri, P., Benassi, M., Matera, S., Peano, D., Ardilouze, C., Batté, L., & Gualdi, S. (2022). On the role of Eurasian autumn snow cover in dynamical seasonal predictions. *Climate Dynamics*, 58(7–8), 2031–2045. <https://doi.org/10.1007/s00382-021-06016-z>
- Santer, B. D., Wigley, T. M., Mears, C. A., Wentz, F., Klein, S. A., Seidel, D. J., et al. (2005). Amplification of surface temperature trends and variability in the tropical atmosphere. *Science*, 309(5740), 1551–1556. <https://doi.org/10.1126/science.1114867>
- Schneider, T., Bischoff, T., & Plotka, H. (2015). Physics of changes in synoptic midlatitude temperature variability. *Journal of Climate*, 28(6), 2312–2331. <https://doi.org/10.1175/jcli-d-14-00632.1>
- Schneider, T., Held, I. M., & Garner, S. T. (2003). Boundary effects in potential vorticity dynamics. *Journal of the Atmospheric Sciences*, 60(8), 1024–1040. [https://doi.org/10.1175/1520-0469\(2003\)60<1024:beipvd>2.0.co;2](https://doi.org/10.1175/1520-0469(2003)60<1024:beipvd>2.0.co;2)
- Screen, J. A., & Simmonds, I. (2010). The central role of diminishing sea ice in recent Arctic temperature amplification. *Nature*, 464(7293), 1334–1337. <https://doi.org/10.1038/nature09051>
- Solomon, S., Rosenlof, K. H., Portmann, R. W., Daniel, J., Davis, S. M., Sanford, T. J., & Plattner, G. (2010). Contributions of stratospheric water vapor to decadal changes in the rate of global warming. *Science*, 327(5970), 1219–1223. <https://doi.org/10.1126/science.1182488>
- Steinman, B. A., Mann, M. E., & Miller, S. K. (2015). Atlantic and Pacific multidecadal oscillations and northern hemisphere temperatures. *Science*, 347(6225), 988–991. <https://doi.org/10.1126/science.1257856>
- Stouffer, R. J., & Manabe, S. (2017). Assessing temperature pattern projections made in 1989. *Nature Climate Change*, 7(3), 163–165. <https://doi.org/10.1038/nclimate3224>
- Stroeve, J. C., Holland, M. M., Meier, W. N., Scambos, T. A., & Serreze, M. C. (2007). Arctic sea ice decline: Faster than forecast. *Geophysical Research Letters*, 34(9), L09501. <https://doi.org/10.1029/2007gl029703>
- Svendsen, L., Keenlyside, N. S., Bethke, I., Gao, Y., & Omrani, N. (2018). Pacific contribution to the early twentieth-century warming in the Arctic. *Nature Climate Change*, 8(9), 793–797. <https://doi.org/10.1038/s41558-018-0247-1>
- Trenberth, K. E. (2015). Has there been a hiatus? *Science*, 349(6249), 691–692. <https://doi.org/10.1126/science.aac9225>
- Trenberth, K. E., & Shea, D. J. (2006). Atlantic hurricanes and natural variability in 2005. *Geophysical Research Letters*, 33(12), L12704. <https://doi.org/10.1029/2006gl026894>
- Tung, K. K., & Zhou, J. (2013). Using data to attribute episodes of warming and cooling in instrumental records. *Proceedings of the National Academy of Sciences*, 110(6), 2058–2063. <https://doi.org/10.1073/pnas.1212471110>
- Wallace, J. M., Zhang, Y., & Renwick, J. A. (1995). Dynamic contribution to hemispheric mean temperature trends. *Science*, 270(5237), 780–783. <https://doi.org/10.1126/science.270.5237.780>
- Wirth, V., Ringer, M., Chang, E. K., & Martius, O. (2018). Rossby wave Packets on the midlatitude waveguide—A review. *Monthly Weather Review*, 146(7), 1965–2001. <https://doi.org/10.1175/mwr-d-16-0483.1>
- Wu, Z., Huang, N. E., Wallace, J. M., Smoliak, B. V., & Chen, X. (2011). On the time-varying trend in global-mean surface temperature. *Climate Dynamics*, 37(3–4), 759–773. <https://doi.org/10.1007/s00382-011-1128-8>
- Wyatt, M. G., Kravtsov, S., & Tsonis, A. A. (2012). Atlantic multidecadal oscillation and northern hemisphere's climate variability. *Climate Dynamics*, 38(5–6), 929–949. <https://doi.org/10.1007/s00382-011-1071-8>
- Xie, P., & Arkin, P. A. (1997). Global precipitation: A 17-year monthly analysis based on gauge observations, satellite estimates, and numerical model outputs. *Bulletin of the American Meteorological Society*, 78(11), 2539–2558. [https://doi.org/10.1175/1520-0477\(1997\)078<2539:gpmaya>2.0.co;2](https://doi.org/10.1175/1520-0477(1997)078<2539:gpmaya>2.0.co;2)
- Xie, Y., Huang, J., & Liu, Y. (2017). From accelerated warming to warming hiatus in China. *International Journal of Climatology*, 37(4), 1758–1773. <https://doi.org/10.1002/joc.4809>
- Xie, Y., Huang, J., & Ming, Y. (2019). Robust regional warming amplifications directly following the anthropogenic emission. *Earth's Future*, 7(4), 363–369. <https://doi.org/10.1029/2018ef001068>
- Xie, Y., Wu, G., Liu, Y., & Huang, J. (2020). Eurasian cooling linked with Arctic warming: Insights from PV dynamics. *Journal of Climate*, 33(7), 2627–2644. <https://doi.org/10.1175/jcli-d-19-0073.1>
- Xie, Y., Wu, G., Liu, Y., Huang, J., & Nie, H. (2022). A dynamic and thermodynamic coupling view of the linkages between Eurasian cooling and Arctic warming. *Climate Dynamics*, 58(9–10), 2725–2744. <https://doi.org/10.1007/s00382-021-06029-8>
- Zhang, P., Wu, Y., Simpson, I. R., Smith, K. L., Zhang, X., De, B., & Callaghan, P. F. (2018). A stratospheric pathway linking a colder Siberia to Barents-Kara Sea ice loss. *Science Advances*, 4(7), eaat6025. <https://doi.org/10.1126/sciadv.aat6025>



Earth's Future

Supporting Information for

**Potential vorticity dynamics explain how extratropical oceans and the Arctic modulate
wintertime land-temperature variations**

Yongkun Xie¹, Jianping Huang¹, Guoxiong Wu^{2,3}, Yimin Liu^{2,3}

¹Collaborative Innovation Center for Western Ecological Safety, Lanzhou University, Lanzhou, China

²State Key Laboratory of Numerical Modeling for Atmospheric Sciences and Geophysical Fluid Dynamics (LASG),
Institute of Atmospheric Physics, Chinese Academy of Sciences, Beijing, China

³College of Earth and Planetary Sciences, University of Chinese Academy of Sciences, Beijing, China

Contents of this file:

Figures S1 to S3

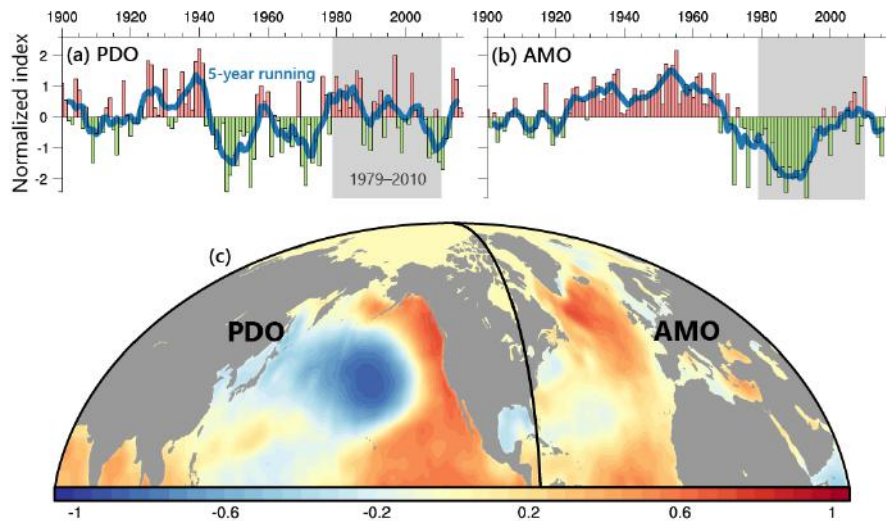


Figure S1. Time series of the normalized DJF mean (a) PDO index and (b) AMO index from 1900 to 2017. Bars indicate the annual results, while the blue curves indicate 5-year running means. Grey rectangle shadings indicate the 1979–2010 period. (c) SST patterns in the positive PDO (left domain) and AMO (right domain) phases that are represented by the linear correlation coefficient between the normalized PDO and AMO indices with SST from 1900 to 2017, respectively.

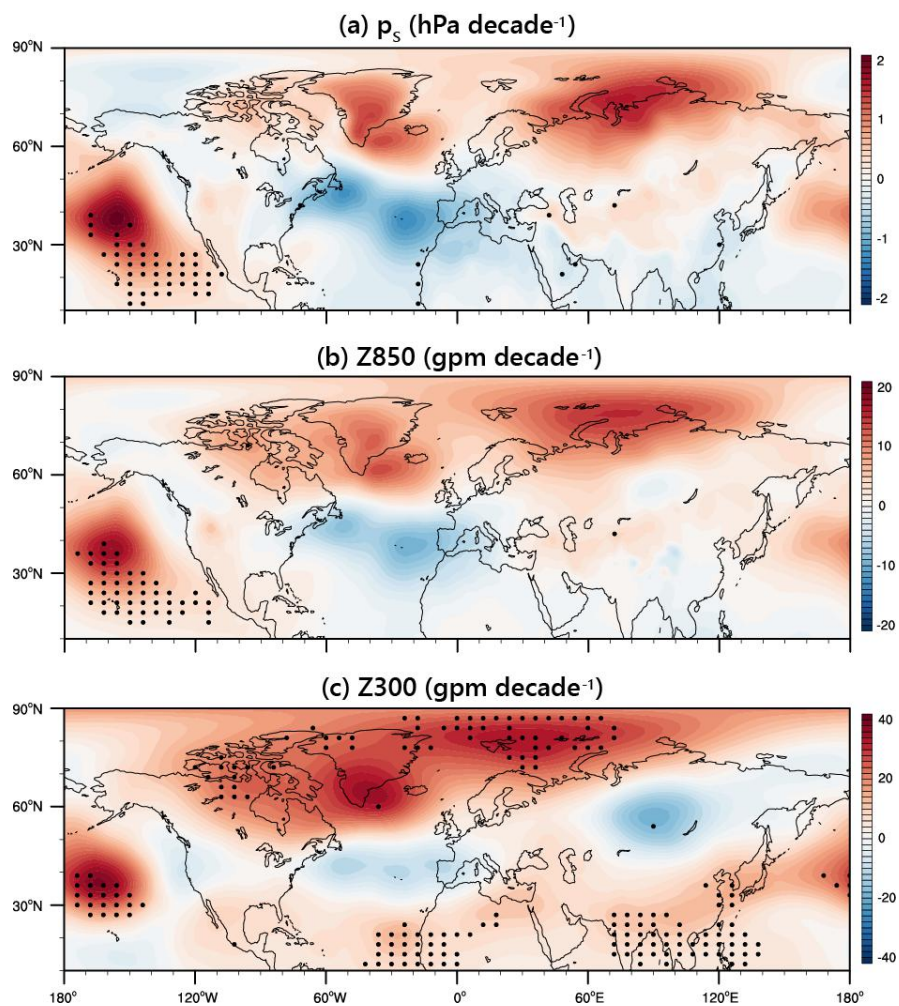


Figure S2. Same as Fig. 1c but for (a) surface pressure (p_s), (b) geopotential height at 850 hPa (i.e., Z850), and (c) geopotential height at 300 hPa (i.e., Z300).

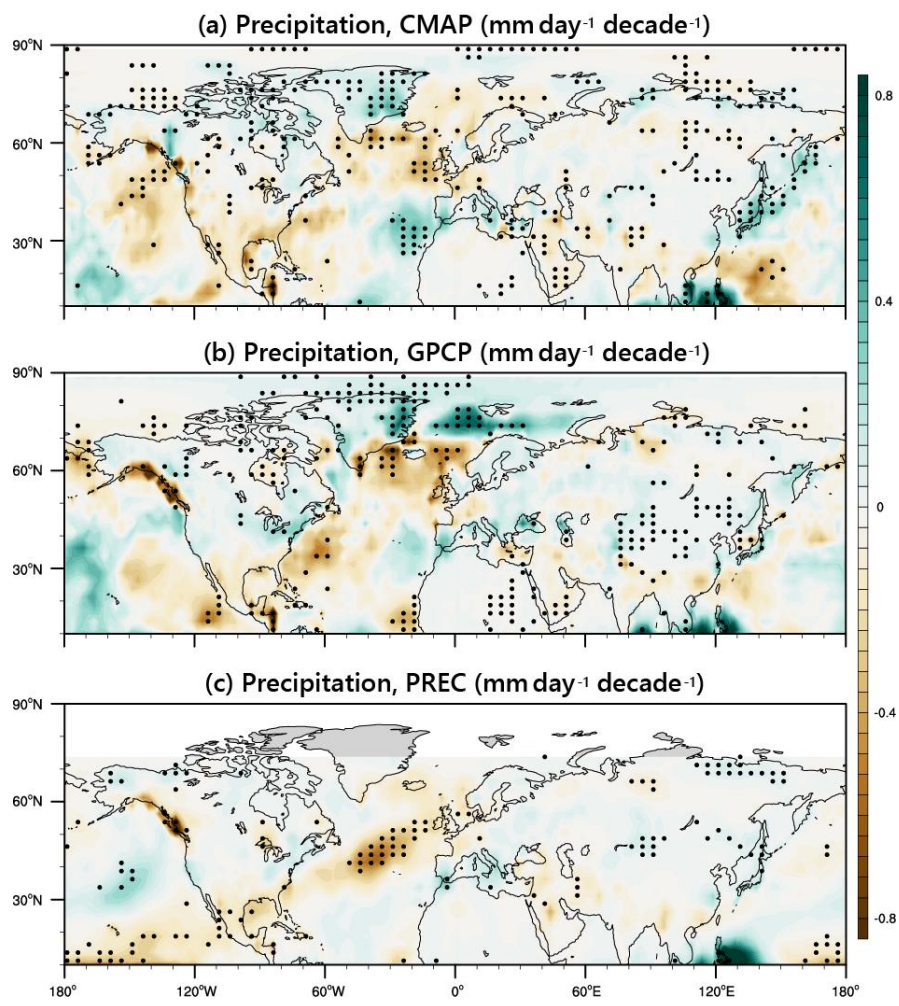


Figure S3. Same as Fig. 2d but for results from (a) CMAP, (b) GPCP, and (c) PREC.